OPEN ACCESS
JOURNAL OF ADVANCED DIELECTRICS
Vol. 12, No. 5 (2022) 2250012 (13 pages)

DOI: 10.1142/S2010135X22500126

Evaluation of dielectric, energy storage and multiferroic properties of $PrFeO_3$–$PbTiO_3$ solid solutions

Mehak Arora*, Shubhpreet Kaur*, Sunil Kumar*, Parambir Singh Malhi†, Mandeep Singh* and Anupinder Singh*,‡

*Department of Physics, Guru Nanak Dev University, Amritsar 143001 Punjab, India

†Department of Chemistry, Guru Nanak Dev University, Amritsar 143001 Punjab, India

‡anupinders@gmail.com

Received 28 June 2022; Revised 1 August 2022; Accepted 4 August 2022; Published 13 October 2022

This work promotes the room temperature energy storage properties of the multiferroics. In this approach, impacts of $PrFeO_3$ doping on PT-based solid solutions ($Pb_{1-x}Pr_xTi_{1-x}Fe_xO_3$, $x = 0.21$, 0.22, 0.23, 0.24, 0.25 and 0.26) have been explored. X-ray diffraction (XRD) patterns were used to estimate the crystallographic parameters, confirming the single phase tetragonal structure. The ferroelectric Curie temperature (T_c^{FE}) is observed to drop from 410 K to below room temperature as the Pr concentration increases. The ferroelectric P-E loops were used to determine the energy storage values at room temperature. The sample $x = 0.24$ achieved the maximum value of energy storage density of 362.25 mJ/cm^3 with the efficiency of 40.5%. The ferroelectric P-E loops were used to determine the energy storage values at room temperature. The validity of magnetoelectric coupling in all samples was confirmed by magneto-dielectric studies and found that the sample $x = 0.24$ shows the maximum response with the coupling coefficient (γ) = 15.54 g^2/emu^2.

Keywords: Ferroelectrics; energy storage; multiferroics; magneto-dielectric; coupling coefficient.

1. Introduction

Multifunctional materials are garnering a lot of attention because of their distinct capabilities.[1–3] They can be used in a variety of ways. One such category, which is being explored the most, is magnetoelectric multiferroics. Multiferroic materials are those substances, which are magnetically and electrically ordered at the same time.[4–6] Partially filled d-orbitals cause magnetic behavior in these materials, whereas ferroelectricity is driven by the unoccupied d-orbitals. The multifunctionality of these materials benefits in memory devices, sensors and energy storage devices.[7–15] Mixed perovskite approach is one of the most frequent ways to make high-performance multiferroics.[16] Ferroelectric oxides having perovskite structure with generic formula ABO_3 possess prominent role in order to explore the areas of research and applications. Among various ferroelectrics, lead titanate (PT) and PT-based materials are in forefront to build mixed perovskite multiferroics. It is the only candidate that has high ferroelectric phase transition, (T_c = 490°C) and high dielectric constant when compared to other ferroelectric materials, allowing for a wide range of applications due to its superior dielectric and ferroelectric properties.[17–19] Transition metal cations such as Fe^{3+}, Mn^{3+}, Ni^{2+}, Co^{2+} are commonly substituted at the Ti-site to provide magnetic behavior. However, substituting transition metal cations increases leakage current in the system. This rise in leakage current is compensated by the addition of rare earth ions (Re^{3+}) to the Pb-site in PT-based materials.[20] Rare earth orthoferrites ($ReFeO_3$, where Re= Sm, La, Gd, Pr, Nd) are commonly used to substitute rare earth cations in ferroelectric perovskites.[21–24] To properly enter into the lattice, the dopant must fulfill the basic requirement (equivalent ionic radii, valence state as the core material).[25] The doping of Pr^{3+} (by following the selection criteria) at Pb-site enhances the electrical and magnetic properties of PT.[26–28] Besides, $PrFeO_3$ (PF) has emerged as a potential alternative in industry due to its high dielectric constant and low dielectric loss.[29,30] It has a G-type antiferromagnetic structure with four Fe and four rare earth ions per unit cell, and like other orthoferrites, it belongs to the *Pbnm* space group.[31] The sharing of Fe-ions with the unit cell's six nearest oxygen ions can be seen in PF's three-dimensional distorted perovskite structure.[32] Such structural aberrations have an impact on magnetic ordering in the suggested material.[33] Singh *et al*. reported the $Pb_{1-x}Pr_xTi_{1-y}Y_yO_3$ where x = 0.02, 0.04, 0.06, 0.08 and $y = 0.02$ and studied its ferroelectric and piezoelectric properties.[34] Samad *et al*. investigated the effect of rare earth ions on lead zirconate titanate (PZT) and obtained that Pr-doped PZT is highly efficient for memory devices.[35] Zou *et al*. studied the microstructure properties of Pr-doped PZT ceramics and proposed that the appropriate amount of Pr enhances the piezoelectric activity in the MPB area.[36] However, little research has been done into the

‡Corresponding author.

mechanism of Pr doping in PT-based material to enhance its multiferroic properties. The primary goal of this research is to investigate the effects of Pr and Fe doping on the A and B-sites of PT-based solid solutions. Owing to the literature survey, $PrFeO_3$–$PbTiO_3$ solid solutions are seen to be a good way to start multiferroic research.

In this work, the synthesis and characterization of $Pb_{1-x}Pr_xTi_{1-x}Fe_xO_3$ ($x = 0.21$, 0.22, 0.23, 0.24, 0.25 and 0.26) have been done. Moreover, the detailed investigation of multiferroic properties has been carried out.

2. Experimental

By using the usual solid state reaction approach, solid solutions of $Pb_{1-x}Pr_xTi_{1-x}Fe_xO_3$ ($x = 0.21$, 0.22, 0.23, 0.24, 0.25 and 0.26) were produced. Pr_6O_{11}, PbO, TiO_2 and Fe_2O_3 were weighed in stoichiometric quantities and mixed thoroughly for 2 h using a mortar pestle. The powder was milled for 24 h after being transferred to vials containing acetone and zirconia balls. The combined powders were calcined at 1000°C for 12 h in a high temperature furnace for phase formation. The powders were then combined with PVA binder of 2 wt.% and formed into circular pellets with a diameter of 10 mm and a thickness of 1 mm using a hydraulic press. To limit weight loss owing to lead volatility, pellets were sintered in a lead environment for 2 h at 1150°C (after optimization tests) using a closed crucible arrangement. These sintered materials' X-ray Diffraction (XRD) data were collected using a Shimadzu (Maxima) diffractometer in the 20°–80° range with a step size of 0.02° and a scan speed of 2°/min using a Cu K anode ($\lambda = 1.54$ Å). All of the samples' surface morphology was studied using a Carl Zeiss FE-SEM (Supra 55) with an InLens detector at 2 kX magnification. To evaluate the density of prepared samples, an Archimedes principle-based setup was used. MicroSense's Vibrating Sample Magnetometer (VSM) EZ9 and Marine India's automatic PE loop tracer was used to measure the electric versus polarization results. The dielectric properties were determined using a KEYSIGHT TECHNOLOGIES impedance analyzer (E4990A), while magneto-dielectric studies were made using an impedance analyzer to measure the dielectric versus frequency in the presence of a magnetic field.

3. Results

3.1. *Structural analysis*

The goal of the phase study was to see how varying levels of Pr affected crystallographic parameters. Figure 1(a) shows the discovered combined patterns of composition $Pb_{1-x}Pr_xTi_{1-x}Fe_xO_3$ ($x = 0.21$, 0.22, 0.23, 0.24, 0.25 and 0.26). Pr^{3+} has successfully penetrated the lattice in all of the samples, which shows a pristine perovskite phase with tetragonal structure. Due to a mismatch in the ionic radii of Pr^{3+} (1.17 Å) and Pb^{2+} (1.49 Å), the peaks are migrating to a higher angle as represented in Fig. 1(b). As the Pr content grows, the diffractographs show a steady elimination of splitting. In order to investigate the detailed information about lattice parameters, the data were refined by Rietveld Refinement using Full Prof software in the 2θ range of 20°–80°. Multiple criteria were considered during the refinement process including zero correction, scale factor, lattice parameters and positional parameters. The background was described using a sixth-order polynomial, while the shape parameter was simulated using the Thompson Cox Hasting Function. Figure 2 depicts the refined graphs for all of the samples. The refined data agree well with the experimental data.

The results reveal that, as the doping value of Pr increases, the *c*/*a* ratio falls. The decrease in crystal tetragonality in the

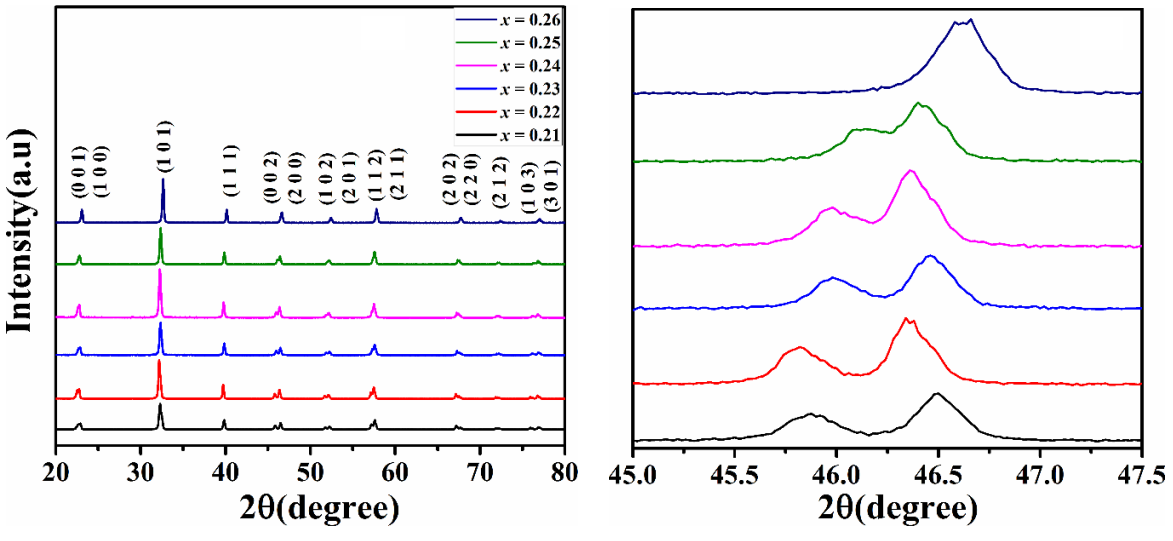

(a) (b)

Fig. 1. (a) The combined patterns of XRD and (b) the migration of peaks between angle 45°–47.5°.

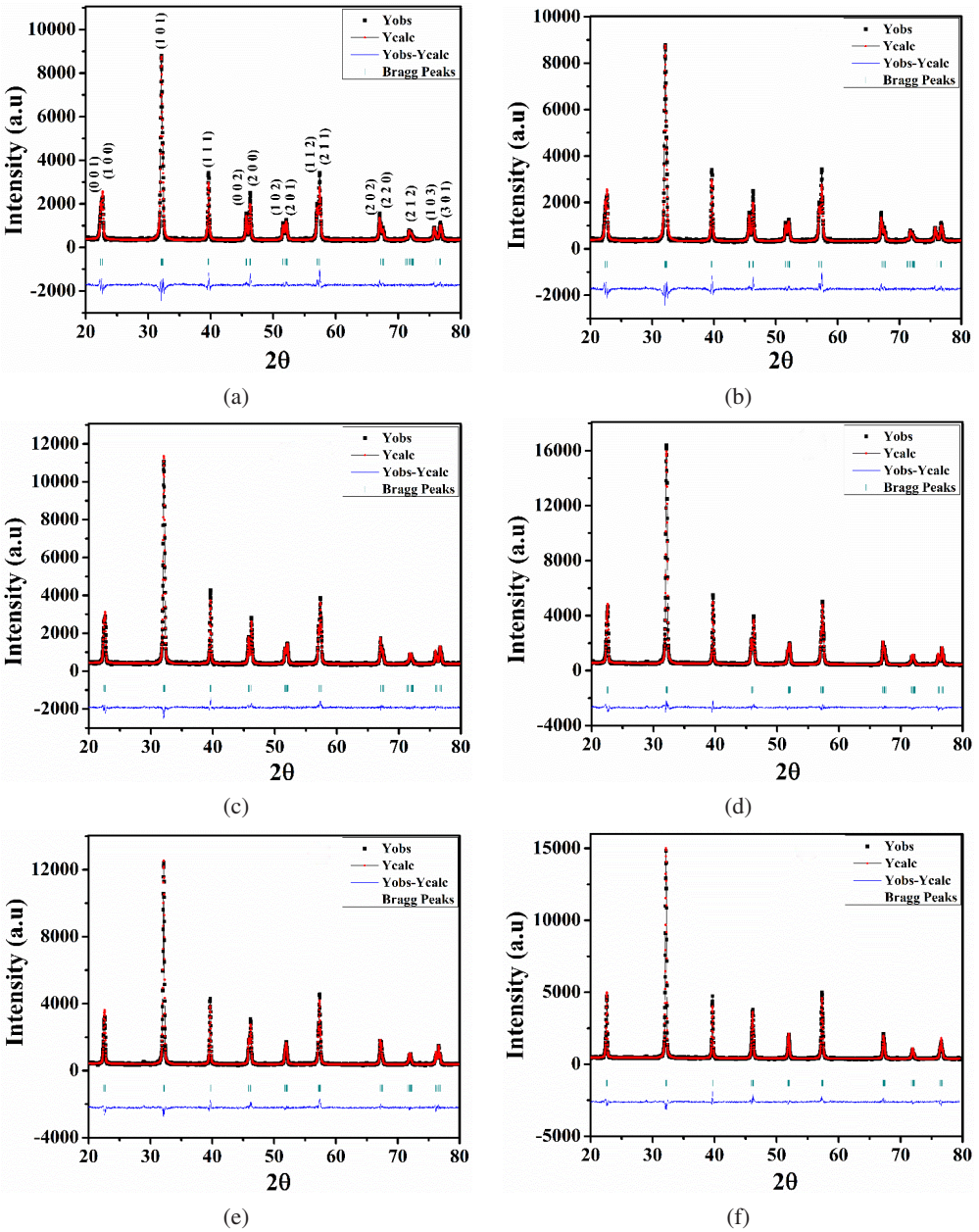

Fig. 2. (a)–(f) The refined XRD graphs of composition $Pb_{1-x}Pr_xTi_{1-x}Fe_xO_3$ ($x = 0.21$, 0.22, 0.23, 0.24, 0.25 and 0.26), respectively.

proposed PT samples is confirmed by this drop in c/a ratio. This could also be due to its high spontaneous stress, as suggested by the $T_s \propto (c/a - 1)$ relation.[37] It can be deduced that the Pr substitution improves the material densification by reducing internal stress, allowing crystallites to form a denser microstructure. All the refined parameters are tabulated in Table 1.

3.2. *Microstructural studies*

Figure 3 shows the images of the collected samples taken from the field emission scanning electron microscopy at a magnification of 10 kX. Along with the images, the histogram displaying the grain size distribution across all samples is also provided. The images demonstrate that the particles have distinct boundaries and are spherical in shape. The photos show that the prepared samples have precise grain development. Image J software was used to determine the average grain size. A lab setup based on the Archimedes principle was used to determine the density of the samples. All of the needed parameters are listed in Table 2, indicating that as the PF quantity is increased, the grain size and experimental density also increases. Figure 4 depicts the EDAX spectrum of one sample of $x = 0.21$ with practically all of the peaks linked with components such as Pb, Fe, Pr and Ti. The results clearly confirm the existence of necessary elements in

Table 1. Parameters obtained from XRD refinement.

Composition	$x = 0.21$	$x = 0.22$	$x = 0.23$	$x = 0.24$	$x = 0.25$	$x = 0.26$
Space Group	**P4mm (tetragonal)**	**P4mm (tetragonal)**	**P4mm (tetragonal)**	**P4mm (tetragonal)**	**P4mm (tetragonal)**	**P4mm (tetragonal)**
a (Å)	3.9212	3.9256	3.9259	3.9267	3.9273	3.9317
c (Å)	3.9711	3.9695	3.9637	3.9575	3.9515	3.9428
Pb/Pr	0/0/0	0/0/0	0/0/0	0/0/0	0/0/0	0/0/0
Fe/Ti	0.5/0.5/0.5045	0.5/0.5/0.4968	0.5/0.5/0.5047	0.5/0.5/0.4916	0.5/0.5/0.5163	0.5/0.5/0.5004
OI	0.5/0/0.0620	0.5/0.5/0.0451	0.5/0.5/0.0430	0.5/0.5/0.038	0.5/0.5/0.0421	0.5/0.5/0.049
OII	0.5/0/0.4487	0.5/0/0.5458	0.5/0/0.5577	0.5/0/0.4918	0.5/0/0.491	0.5/0/0.6013
V(Å^3)	61.2603	61.1693	61.0940	60.9971	60.9458	60.9391
Polarization (μC/cm^2)	9.66	7.42	6.83	5.22	5.08	2.05
R_{exp}	8.83	8.01	8.57	7.34	8.55	8.36
χ^2 (GOF)	4.40	2.96	2.58	3.15	2.97	2.87

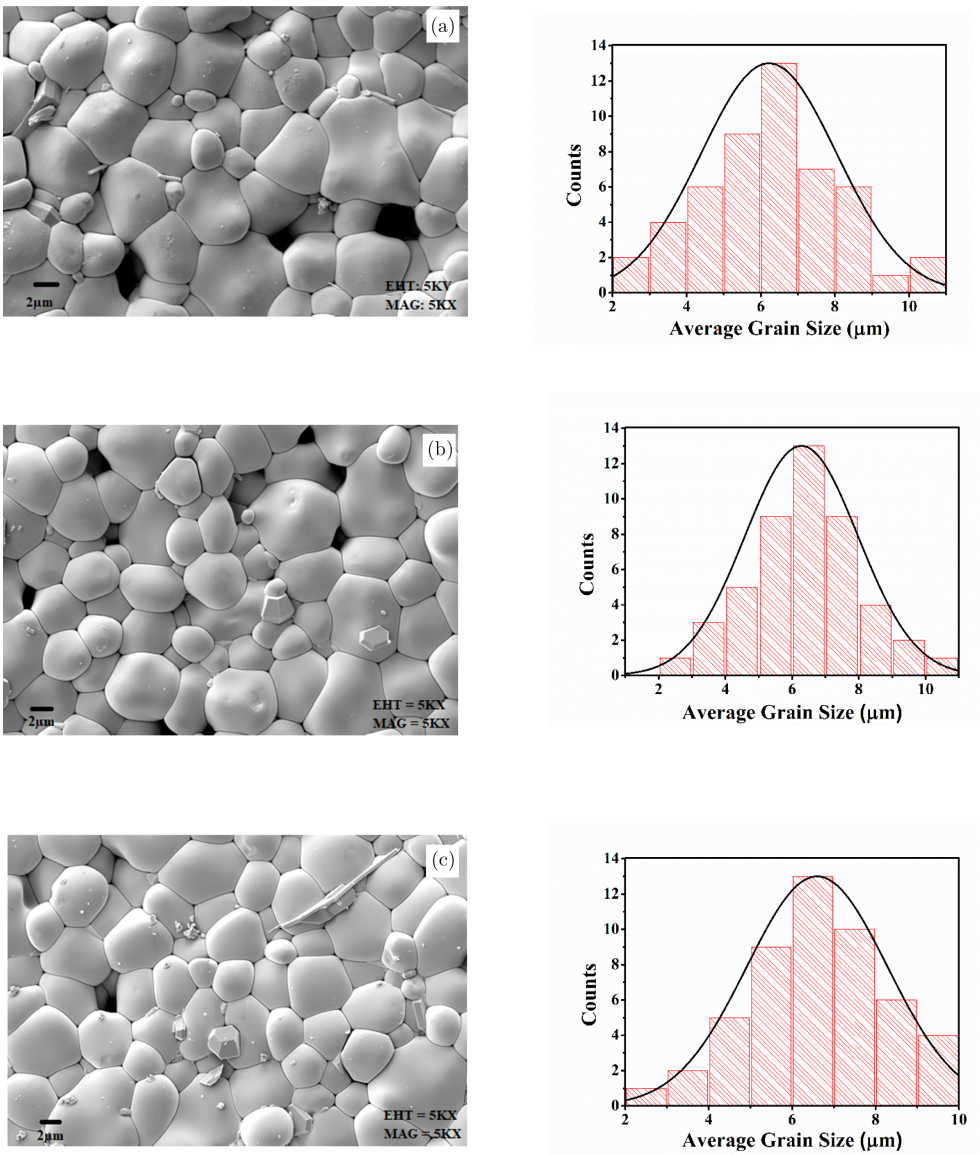

Fig. 3. (a–f) The FE-SEM images of composition $Pb_{1-x}Pr_xTi_{1-x}Fe_xO_3$ ($x = 0.21$, 0.22, 0.23, 0.24, 0.25 and 0.26), respectively.

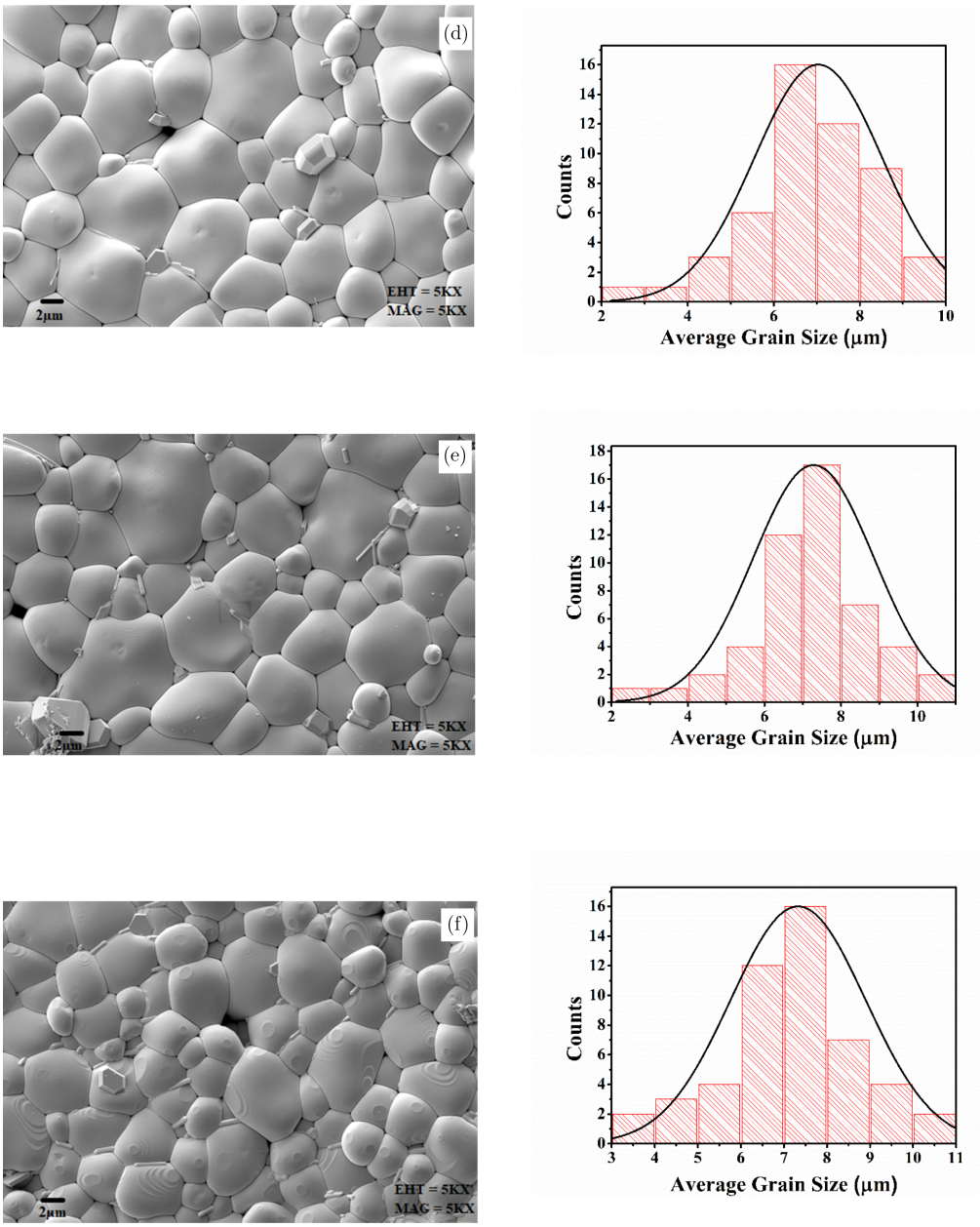

Fig. 3. (*Continued*)

Table 2. Data acquired after analysis from FE-SEM micrographs.

Sample	Average grain size (μm)	Standard deviation (σ)	Experimental density (g cm^{-3})	Theoretical density (g cm^{-3})
$x = 0.21$	6.218	1.831	5.6839	7.84
$x = 0.22$	6.280	1.698	6.1317	7.86
$x = 0.23$	6.599	1.686	6.899	7.87
$x = 0.24$	7.035	1.487	7.022	7.89
$x = 0.25$	7.281	1.586	7.310	7.90
$x = 0.26$	7.329	1.567	7.585	7.92

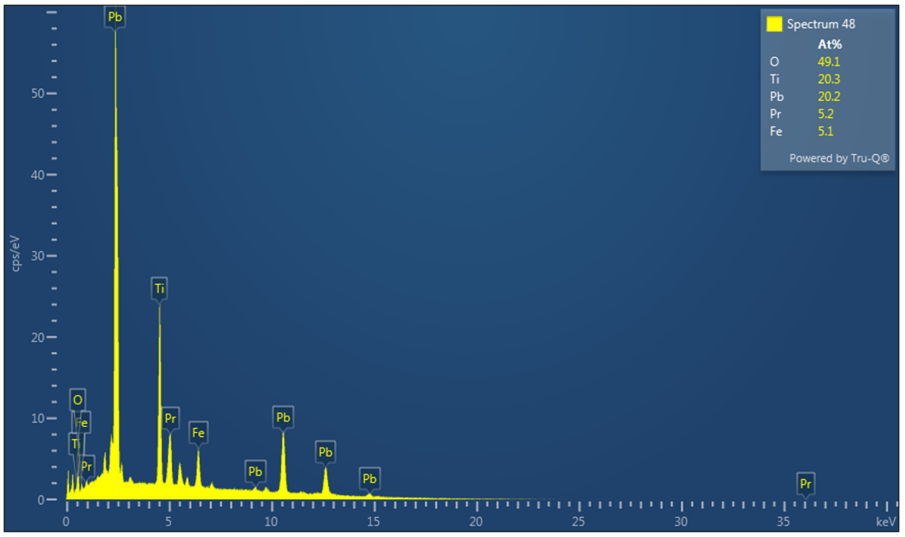

Fig. 4. The EDAX spectrum of composition $Pb_{1-x}Pr_xTi_{1-x}Fe_xO_3$ ($x = 0.21$).

the composition. As a result of the microstructural study, this material is $PbTiO_3$ substituted by Pr and Fe.

3.3. *Dielectric properties*

Figure 5 depicts the acquired temperature versus dielectric constant (ε') plots for various Pr compositions across a frequency range of 1–100 kHz. There is no dielectric deviation in the low-temperature area, as in ordinary ferroelectrics, and the dielectric constant climbs steadily below the Curie temperature before dropping. The dielectric constant exhibits this behavior at higher temperatures due to the creation of additional thermal energy, which improves the movement of charge carriers and thereby boosts the hopping rate.

Furthermore, as Pr concentration rises, the ferroelectric Curie temperature (T_c^{FE}) drops from 410 K to below room temperature. It is linked to lower tetragonality in the samples, which lowers the internal stress and as a result, lowers the transition temperature.[38] Figure 6 depicts the variation in dielectric loss (tanδ) anomalies as a function of temperature for all samples. Structure irregularities and grain orientations are the primary causes of loss in the samples.[39,40] The calculated values of T_c^{FE}, ε', tanδ and c/a are given in Table 3.

3.4. *Ferroelectric properties*

The modulation of polarization versus electric field at room temperature (referred as PE loops) was studied to ensure ferroelectric behavior in all the samples in $Pb_1\_xPrxTi_1\_xFexO_3$ ($x = 0.21$–0.26). The polarization in lead-based materials is related to the hybridization in 3d and 2p states of titanium and oxygen ions.[41] As seen in Figs. 7(a)–7(f), the loops possess symmetric behavior, which demonstrates that the trapped charges are dispersed uniformly across all the samples.[42] There is an appearance of lossy behavior in sample $x = 0.26$, which may be due to the increase in the leakage current due to rise in the Fe concentration. Hence, the leakage current can deteriorate the ferroelectric behavior.[43] Figure 7(g) illustrates the relationship between c/a ratio and remnant polarization (P_r) with composition (x) and found that the value of P_r for $x = 0.21$ drops from 14.42 μC/cm^2 to 5.17 μC/cm^2, while the result of coercive field (E_c) declines from 0.21 to 0.24 and then increases as given in Fig. 7(h). This could be because of the cell content that has a smaller atomic displacement, which results in the softening of the material.[44] The phase structure of the sample $x = 0.26$ is different to others. It is because that the c/a ratio for this sample is almost equal to 1, which leads to have the lowest tetragonality from the other samples. Moreover, lowering the tetragonality leads to decrease in the dielectric constant value at Curie temperature (T_c^{FE}) and lossy behavior of the ferroelectric loop of the sample.

3.5. *Energy storage analysis*

The ferroelectric loops also provide the information about the energy storage properties of the dielectric materials. The total energy stored in the material can be linked with the application of electric field. The change in the value of electric field corresponds to discharge/charge process as shown in Fig. 8. The recoverable energy density (area ABCA, blue color) is used to calculate the energy storage in the material as follows:

$$W_{rec} = \int_{P_r}^{P_{max}} E\, dP, \tag{1}$$

where P_{max} is the maximum attained polarization, P_r is the remnant polarization and E is the applied value of the electric field. Moreover, the area A′BAA′ (green color) is termed as the energy loss density (W_{loss}), which arises from the

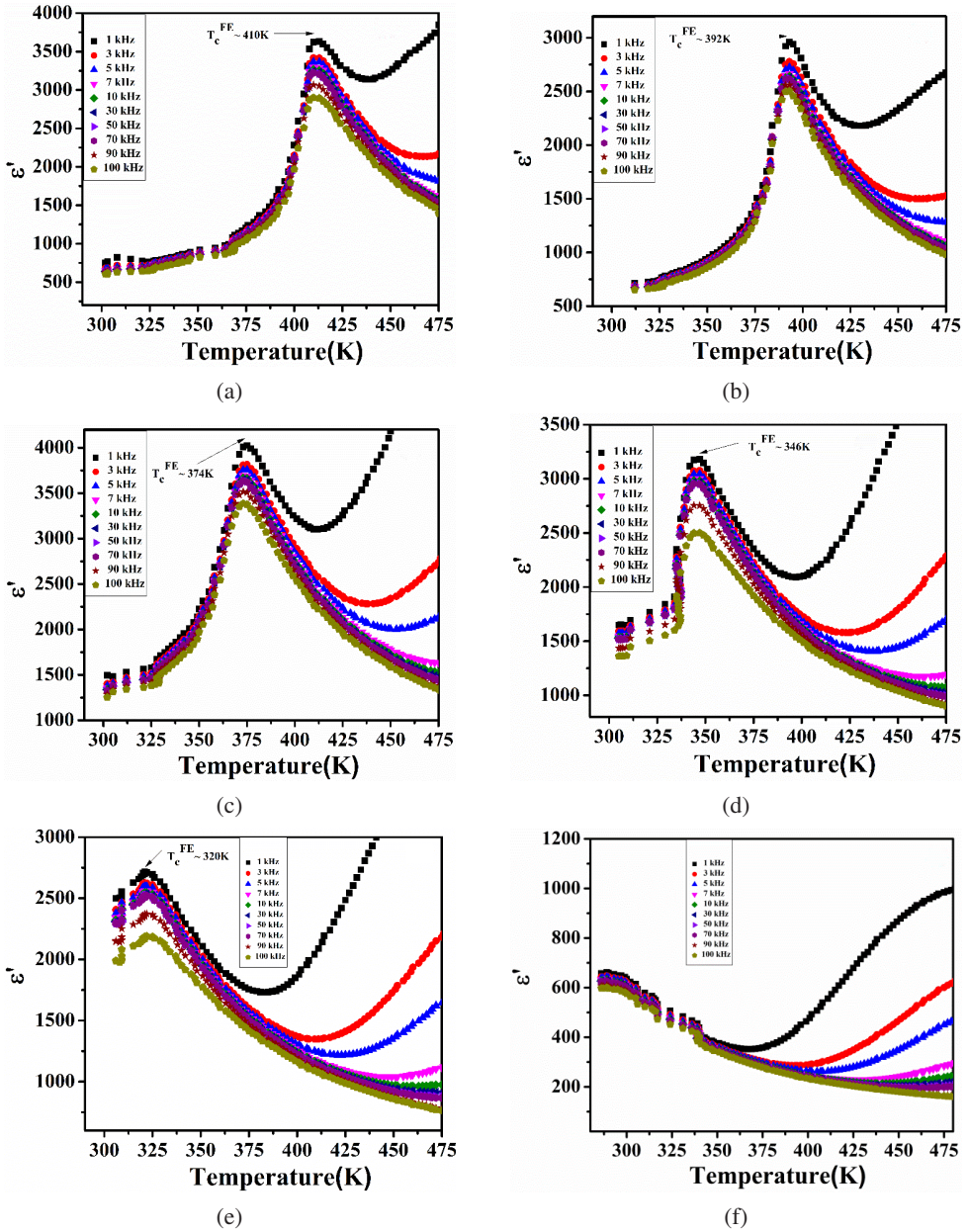

Fig. 5. (a)–(f) The obtained temperature versus dielectric constant (ε') plots of composition $Pb_{1-x}Pr_xTi_{1-x}Fe_xO_3$ (x = 0.21, 0.22, 0.23, 0.24, 0.25 and 0.26), respectively.

dissipation of heat in the dielectrics.[45] The energy storage efficiency (η) of the material can be obtained by

$$\eta = \frac{W_{rec}}{W_{rec} + W_{loss}} \times 100\%. \quad (2)$$

Figure 9 represents the obtained values of W_{rec}, W_{loss} and η with respect to electric field calculated from Eqs. (1) and (2). Table 4 shows that the maximum value of the energy storage density (W_{rec} = 362.25 mJ/cm^3) is given by sample x = 0.24 with an efficiency of 40.5% at 50 kV/cm. As given in Eq. (1), material can possess higher energy storage for which change in polarization with electric field i.e., $\Delta P = P_{max} - P_r$ is maximum.[46] For higher value of ΔP, P_{max} should be maximum keeping the lower value of P_r. Recall that sample x = 0.24 has shown the minimum value of P_r as depicted in Fig. 7(g) leading to higher value of energy density.

3.6. *Magnetic analysis*

For the magnetic analysis, the variation in magnetization (M) with respect to applied magnetic field (H) has been studied. Figure 10 represents the M-H graphs for $Pb_{1-x}PrxTi_{1-x}Fexo_3$ (x = 0.21–0.26) samples. The creation of oxygen vacancies during Fe^{3+} ion doping in Ti^{4+} sites is ascribed to the magnetic behavior of the samples.[47] Moreover, the five unpaired

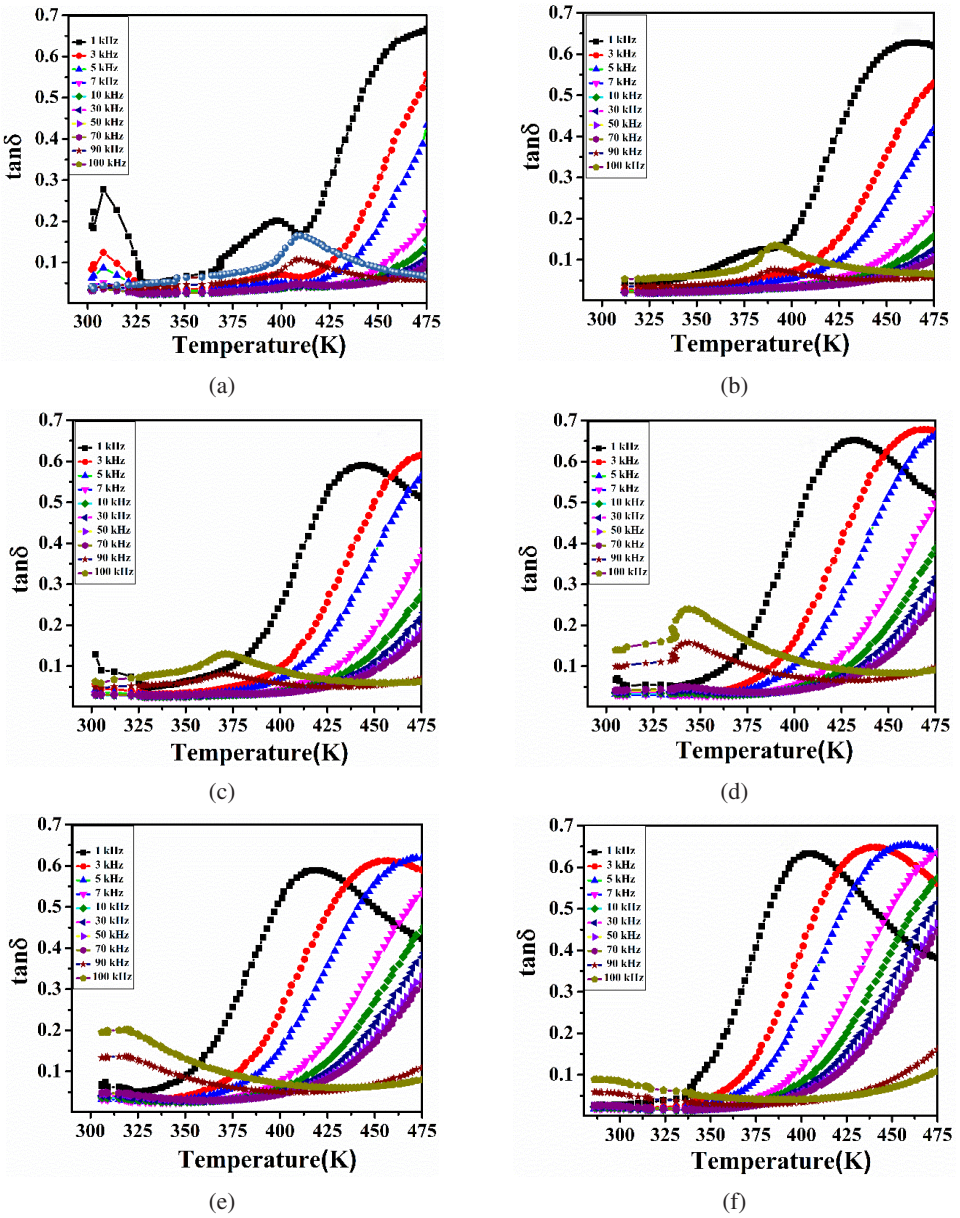

Fig. 6. (a)–(f) The variation in dielectric loss (tanδ) anomalies as a function of composition $Pb_{1-x}Pr_xTi_{1-x}Fe_xO_3$ ($x = 0.21$, 0.22, 0.23, 0.24, 0.25 and 0.26), respectively.

Table 3. The calculated values of T_c^{FE}, ε', tanδ and c/a of composition $Pb_{1-x}Pr_xTi_{1-x}Fe_xO_3$ ($x = 0.21$, 0.22, 0.23, 0.24, 0.25 and 0.26), respectively, at frequency 1 kHz.

Composition	T_c^{FE} (in K)	ε' (at T_c^{FE})	Tanδ (at T_c^{FE})	c/a
$x = 0.21$	410	3621	0.169	1.0127
$x = 0.22$	392	2958	0.132	1.0111
$x = 0.23$	374	4008	0.097	1.0096
$x = 0.24$	346	3181	0.060	1.0078
$x = 0.25$	320	2707	0.053	1.0061
$x = 0.26$	—	—	—	1.0028

d-shell electrons of Fe^{3+} ion also gives the confirmation of the magnetic order in all the samples. The increase in remnant magnetization (M_r) with enhanced coercivity is clearly visible from the figure. Evidently, increasing Fe content from PF concentration is directly correlated with improved magnetic behavior of these samples. The observed values of remnant magnetization obtained from the M-H data are tabulated in Table 5.

3.7. *Magneto-dielectric study*

As indicated in Fig. 11, the validity of magnetoelectric (ME) coupling in all samples was determined using ε' versus

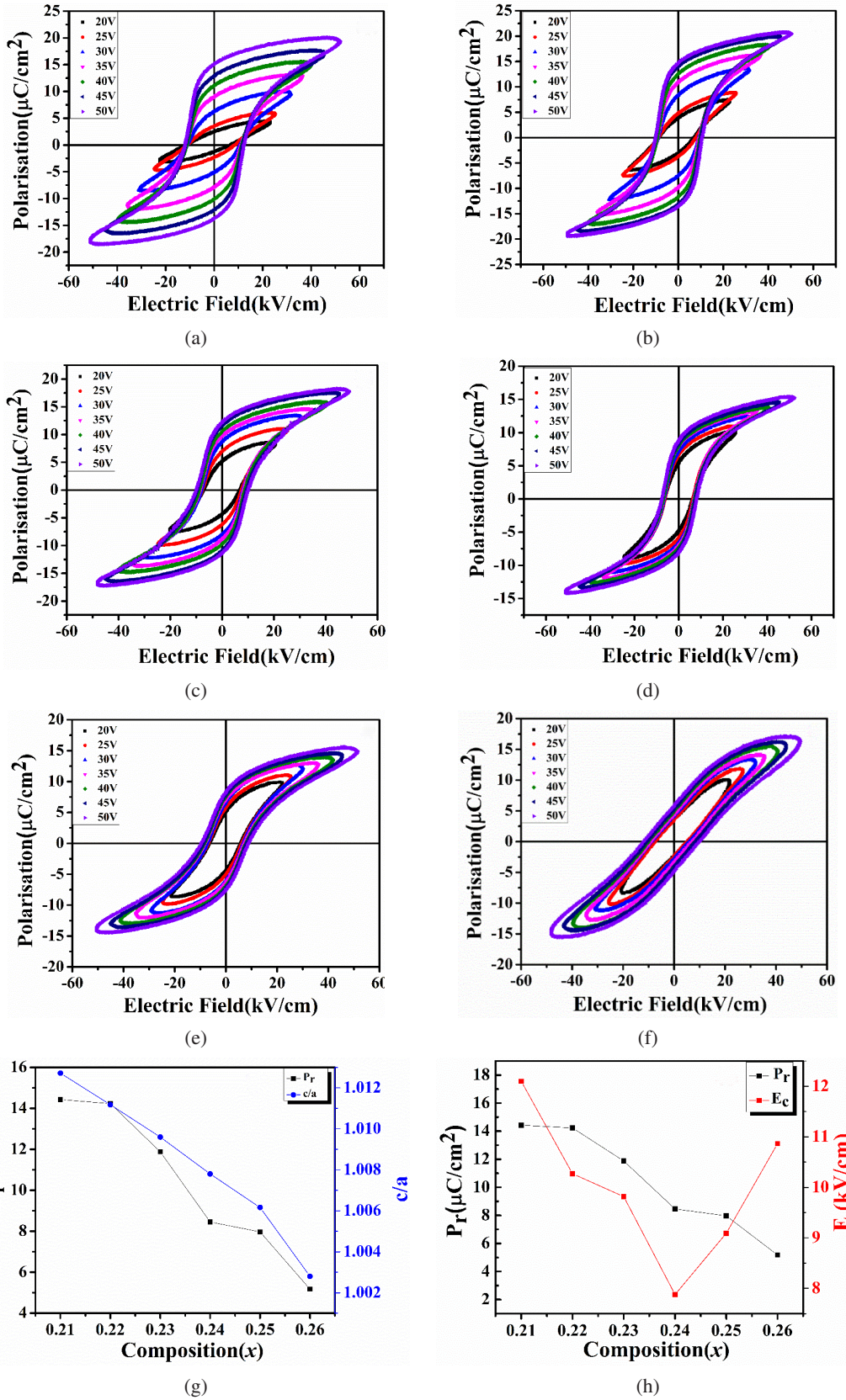

Fig. 7. (a)–(f) PE loops of composition $Pb_{1-x}Pr_xTi_{1-x}Fe_xO_3$ (x = 0.21, 0.22, 0.23, 0.24, 0.25 and 0.26), respectively, (g) variation between c/a ratio and remnant polarization (P_r) with composition (x) and (h) variation between coercive field (E_c) and remnant polarization (P_r) with composition (x).

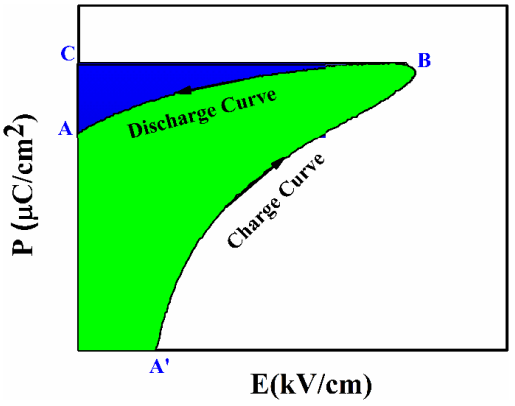

Fig. 8. Diagrammatic representation of charge–discharge process for assessing their energy storage capabilities.

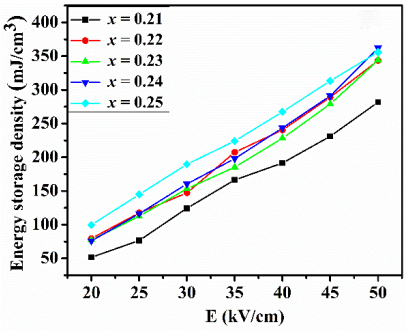

(a)

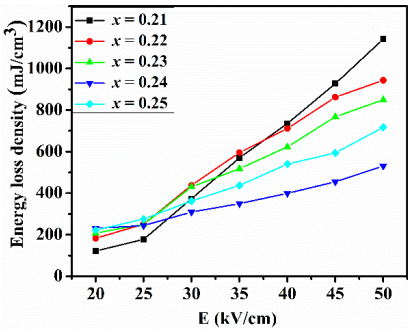

(b)

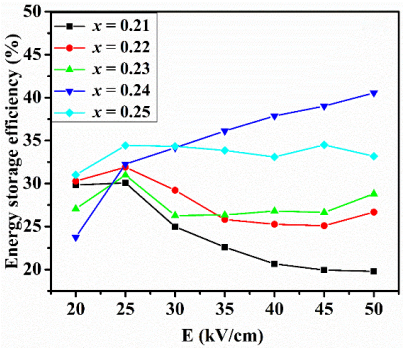

(c)

Fig. 9. (a)–(c) The obtained values of W_{rec}, W_{loss} and η with respect to applied electric field.

Table 4. The calculated values of W_{rec}, W_{loss} and η of proposed samples at room temperature at 50 kV/cm.

Composition	W_{rec} (mJ/cm^3)	W_{loss} (mJ/cm^3)	η (%)
$x = 0.21$	281.61	1141.58	19.71
$x = 0.22$	343.52	943.54	26.68
$x = 0.23$	344.05	849.83	28.81
$x = 0.24$	362.25	531.09	40.55
$x = 0.25$	356.01	716.78	33.18

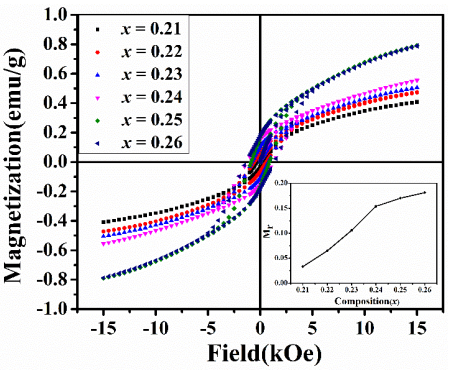

Fig. 10. The combined *M-H* graphs for composition $Pb_{1-x}Pr_x$-$Ti_{1-x}Fe_xO_3$ ($x = 0.21$, 0.22, 0.23, 0.24, 0.25 and 0.26), respectively.

Table 5. The observed values of remnant magnetization (M_r) obtained from the *M-H* data.

Composition (x)	Remnant magnetization (M_r) (emu/g)
$x = 0.21$	0.03
$x = 0.22$	0.06
$x = 0.23$	0.10
$x = 0.24$	0.15
$x = 0.25$	0.17
$x = 0.26$	0.18

frequency measurements with different magnetic fields (0 T, 0.5 T, 1 T and 1.5 T). The samples show magnetoelectric coupling only up to $x = 0.25$ as there was a variation in the value of ε' with a change in the magnetic field. A visible decrease in the value of ε' has been observed in the figure. This decrement in the value of ε' also indicates a negative magneto-dielectric response in the samples. The simultaneous generation of stress in the magnetic and ferroelectric domains by an externally applied magnetic field is responsible for the change in dielectric permittivity of the material.[48,49] The magneto-dielectric response can be calculated as follows:

$$\text{MDR Response} = \frac{\varepsilon'(H) - \varepsilon'(0)}{\varepsilon'(0)} \times 100\%, \quad (3)$$

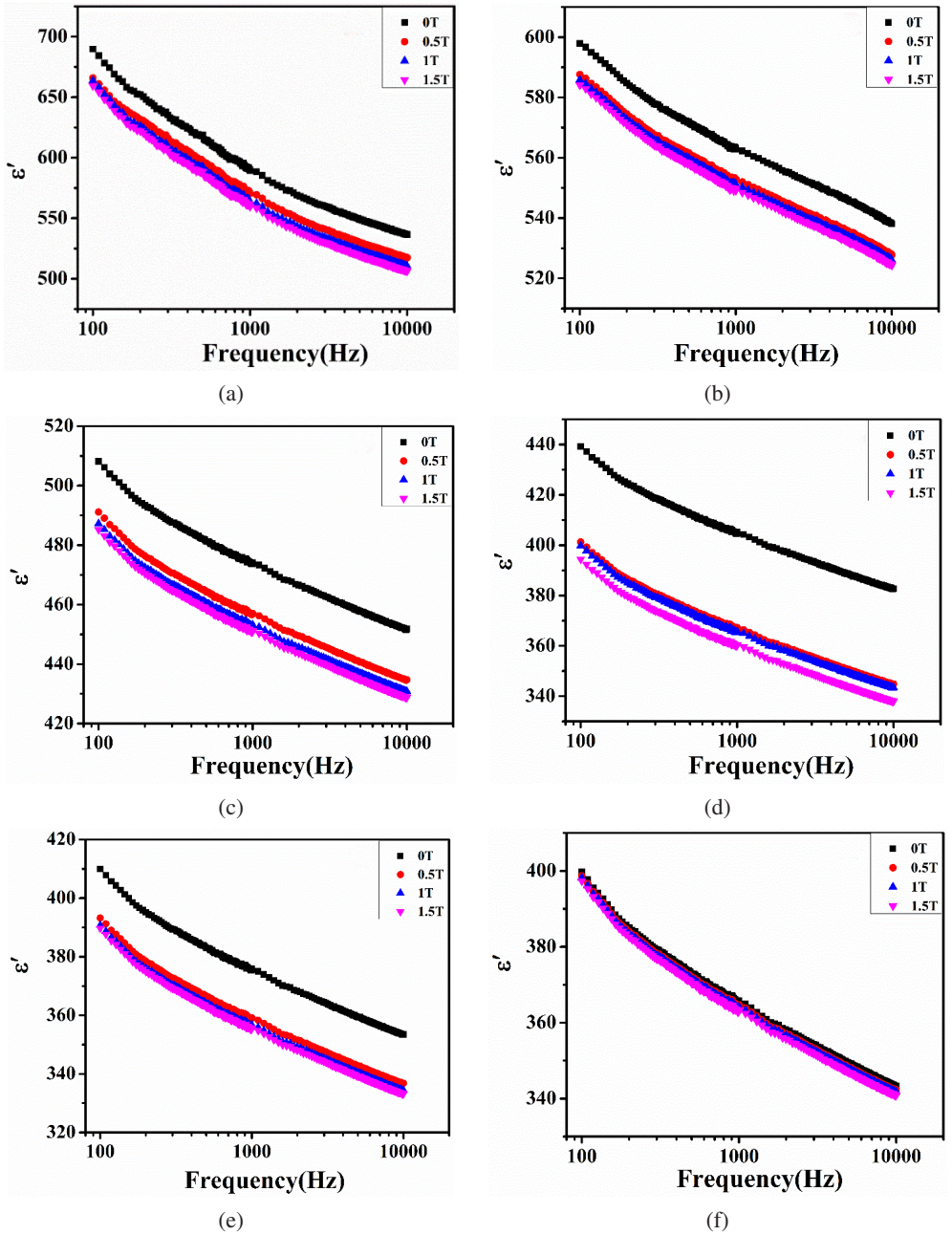

Fig. 11. (a)–(f) The ε' versus frequency measurements at different magnetic fields (0T, 0.5T, 1T and 1.5T) of composition $Pb_{1-x}Pr_xTi_{1-x}Fe_xO_3$ ($x = 0.21$, 0.22, 0.23, 0.24, 0.25 and 0.26), respectively.

where $\varepsilon'(H)$ and $\varepsilon'(0)$ represent the dielectric constant with and without magnetic field, respectively. From the response value, it is found that $x = 0.24$ shows maximum magneto-dielectric effect. Further to find the magneto-electric coefficient (γ), Ginzburg–Landau–Devonshire theory[50] is used in multiferroic system as follows:

$$\Phi = \Phi_o + \alpha P^2 + \frac{\beta}{2} P^4 - PE + \alpha' P^2 + \frac{\beta'}{2} M^4 - MH + \gamma P^2 M^2 . \quad (4)$$

Here, α, α', β, β' and γ are the coefficients of ME coupling, P and M indicate the polarization and magnetization, respectively, whereas P^2m^2 gives the measure of ME coupling. The influence of a magnetic field on the dielectric constant can be calculated as $\frac{\varepsilon'(H)-\varepsilon'(0)}{\varepsilon'(0)} \sim \gamma M^2$. The value of γ can be estimated by linear fitting of above equation for $x = 0.21$, 0.22, 0.23, 0.24 and 0.25 samples and the values are tabulated in Table 6. According to the table, the value of γ is the highest for the $x = 0.24$ sample, indicating that it has the best multiferroic characteristics. The maximum value of γ for sample $x = 0.24$ is due to the presence of ferroelectric as well as

Table 6. The values of MDR % at different magnetic field and observed value of γ.

Composition (x)	MDR (%) at 0.5 T	MDR (%) at 1 T	MDR (%) at 1.5 T	γ (g^2/emu^2)
$x = 0.21$	3.46	3.76	4.41	8.94
$x = 0.22$	3.35	4.10	4.51	10.8
$x = 0.23$	1.71	2.0	2.30	11.1
$x = 0.24$	8.53	9.07	11.56	15.54
$x = 0.25$	5.65	6.01	6.53	11.8

magnetic domains. Since sample $x = 0.24$ has shown maximum magnetization along with ferroelectric behavior, this sample exhibited maximum coupling phenomenon. Also, it is worth mentioning that this sample has also shown the maximum energy storage density.

4. Conclusion

$Pb_{1-x}Pr_xTi_{1-x}Fe_xO_3$ ($x = 0.21$, 0.22, 0.23, 0.24, 0.25 and 0.26) has been prepared by solid-state reaction route. The structural, energy storage and magnetoelectric properties are studied in depth in this work. The phase analysis and dielectric studies supported the creation of hard ceramics in $PrFeO_3$-doped PT solid solutions. It has been proven that the tetragonality decreases with increase in doping concentration. With increasing Pr content, the value of remnant polarization is observed to be diminished from 14.42 μC/cm^2 to 5.17 μC/cm^2 for $x = 0.21$–0.26 sample. The sample $x = 0.24$ achieved the maximum value of energy storage density of 362.25 mJ/cm^3 with the efficiency of 40.5%. The magnetic character of the prepared samples increases with a rise in the amount of Fe. The magneto-dielectric studies confirmed the presence of multiferroic nature in the proposed samples. The maximum response was exhibited by $x = 0.24$ sample with the coupling coefficient (γ) value of 15.54 g^2/emu^2.

Acknowledgments

The authors wish to thank the Centre for Emerging Life Sciences, GNDU for providing characterization facilities (VSM). Mehak Arora also wishes to thank Rusa-2.0 and DST-SERB for providing financial support.

References

[1]M. Bibes and A. Barthélémy, Multiferroics: Towards a magnetoelectric memory, *Nat. Mater.* **7**, 425 (2008).
[2]C. W. Nan, M. I. Bichurin, S. Dong, D. Viehland and G. Srinivasan, Multiferroic magnetoelectric composites: Historical perspective, status, and future directions, *J. Appl. Phys.* **103**, 031101 (2008).
[3]N. A. Spaldin, S. Cheong and R. Ramesh, Multiferroics: Past, present, and future Additional resources for Physics Today, *Cit. Phys. Today* **63**, 38 (2010).
[4]G. A. Smolenskii and I. E. Chupis, Ferroelectromagnets, *Sov. Phys. - Uspekhi* **25**, 415 (1982).
[5]J. P. Velev, S. S. Jaswal and E. Y. Tsymbal, Multi-ferroic and magnetoelectric materials and interfaces, *Philos. Trans. R. Soc. A* **369**, 3069–3097 (2011).
[6]M. Gajek *et al.*, Tunnel junctions with multiferroic barriers, *Nat. Mater*. **6**, 296 (2007).
[7]J. M. Chem, Applications of magnetoelectrics, *J. Mater. Chem*. **22**, 4567 (2012).
[8]D. Storage, Multiferroic memories model interfaces, *Nat. Mater*. **6**, 256 (2007).
[9]N. A. Hill, Why are there so few magnetic ferroelectrics? *J. Phys. Chem. B* **104**, 6694 (2000).
[10]D. Khomskii, Classifying multiferroics: Mechanisms and effects, *Physics (College. Park. Md).* **2**, 2–8 (2009).
[11]K. C. Verma, R. K. Kotnala and N. S. Negi, Improved dielectric and ferromagnetic properties in Fe-doped $PbTiO_3$ nanoparticles at room temperature, *Appl. Phys. Lett.* **92**, 152902 (2008).
[12]C. M. Leung, J. Li, D. Viehland and X. Zhuang, A review on applications of magnetoelectric composites: From heterostructural uncooled magnetic sensors, energy harvesters to highly efficient power converters, *J. Phys. D. Appl. Phys.* **51**, 263002 (2018).
[13]W. Eerenstein, N. D. Mathur and J. F. Scott, Multiferroic and magnetoelectric materials, *Nature* **442**, 759 (2006).
[14]C. Schmitz-Antoniak *et al.*, Electric in-plane polarization in multiferroic $CoFe_2O_4/BaTiO_3$ nanocomposite tuned by magnetic fields, *Nat. Commun.* **4**, 2051 (2013).
[15]L. Zhang, S. Jiang, B. Fan and G. Zhang, Enhanced energy storage performance in (Pb0.858Ba0.1La0.02Y0.008)(Zr0.65Sn0.3Ti0.05)O_3-(Pb0.97La0.02)(Zr0.9Sn0.05Ti0.05)O_3 anti-ferroelectric composite ceramics by spark plasma sintering, *J. Alloys Compd.* **622**, 162 (2015).
[16]S. Kumar *et al.*, Correlation between multiferroic properties and processing parameters in $NdFeO_3$-$PbTiO_3$ solid solutions, *J. Alloys Compd.* **764**, 824 (2018).
[17]C. Zhang *et al.*, Multiferroicity in SmFeO3 synthesized by hydrothermal method, *J. Alloys Compd.* **665**, 152 (2016).
[18]K. Aizu, Possible species of ferromagnetic, ferroelectric, and ferroelastic crystals, *Phys. Rev. B* **2**, 754 (1970).
[19]H. Schmid, Multi-ferroic magnetoelectrics, *Ferroelectrics* **162**, 317 (1994).
[20]A. Singh and R. Chatterjee, Magnetization induced dielectric anomaly in multiferroic $LaFeO_3$-$PbTiO_3$ solid solution, *Appl. Phys. Lett.* **93**, 1 (2008).
[21]J. E. Garcia, V. Gomis, R. Perez, A. Albareda and J. A. Eiras, Unexpected dielectric response in lead zirconate titanate ceramics: The role of ferroelectric domain wall pinning effects, *Appl. Phys. Lett.* **91**, 1 (2007).
[22]H. Jaffe, Piezoelectric ceramics, *J. Am. Ceram. Soc.* **41**, 494 (1958).
[23]A. V. Kimel *et al.*, Ultrafast non-thermal control of magnetization by instantaneous photomagnetic pulses, *Nature* **435**, 655 (2005).
[24]D. Bossini *et al.*, Time-resolved nonlinear infrared spectroscopy of samarium ions in $SmFeO_3$, *Phys. Rev. B. Condens. Matter Mater. Phys.* **87**, 2 (2013).
[25]A. Pelaiz Barranco, F. Calderon Piñar, O. Perez Martinez and E. Torres Garcia, Effects of MnO_2 additive on the properties of PbZrO$_3$-PbTiO$_3$-PbCu$_1$/4Nb$_3$/4O$_3$ ferroelectric ceramic system, *J. Eur. Ceram. Soc.* **21**, 523 (2001).
[26]K. T. Kubra *et al.*, Synthesis and characterization of novel Pr_6O_{11}/Mn_3O_4 nanocomposites for electrochemical supercapacitors, *Ceram. Int.* **45**, 6819 (2019).
[27]R. D. Shanon, Revised effective ionic radii and systematic studies of interatomie distances in halides and chaleogenides, *Acta Cryst.* **32**, 751 (1976).

[28]W. Cao *et al.*, Effect of Pr6O11 doping on the microstructure and electrical properties of ZnO varistors, *Ceram. Int.* **45**, 24777 (2019).
[29]S. V. Trukhanov, Investigation of stability of ordered manganites, *J. Exp. Theor. Phys.* **101**, 513 (2005).
[30]S. V. Trukhanov *et al.*, Study of A-site ordered PrBaMn2O6-δ manganite properties depending on the treatment conditions, *J. Phys. Condens. Matter* **17**, 6495 (2005).
[31]J. Park and T. Kimura, Competition between lattice distortion and charge dynamics for the charge carriers of double-layered manganites, *Phys. Rev. B Condens. Matter Mater. Phys.* **58**, R13330 (1998).
[32]A. Moodenbaugh, B. Nielsen and S. Sambasivan, Hole-state density of across the insulator/metal phase boundary, *Phys. Rev. B Condens. Matter Mater. Phys.* **61**, 5666 (2000).
[33]M. Marezio and P. D. Dernier, The bond lengths in $LaFeO_3$. *Mater. Res. Bull.* **6**, 23 (1971).
[34]K. Singh, V. Singh, R. Gupta and K. Bamzai, Structural, dielectric, piezoelectric and ferroelectric behavior of rare earth double doped lead titanate ceramics synthesized by solid state method, *J. Appl. Phys.* **6**, 8 (2014).
[35]R. Samad, M. ud D. Rather, K. Asokan and B. Want, Structural, dielectric and ferroelectric properties of rare earth substituted lead zirconate titanate, *J. Mater. Sci. Mater. Electron.* **29**, 4226 (2018).
[36]L. Zou *et al.*, Microstructure and electric properties of Pr-doped $Pb(Zr0.52Ti0.48)O_3$ ceramics, *Ceram. Int.* **47**, 19328 (2021).
[37]T. Takahashi, Lead titanate ceramics with large piezoelectric anisotropy and their applications, *Ceram. Bull.* **69**, 691 (1990).
[38]K. Okazaki, Mechanical behavior of ferroelectric ceramics, *Am. Ceram. Soc. Bull.* **63**, 1150 (1984).
[39]K. Prasad, R. Sati and R. N. P. Choudhary, Synthesis and electrical studies of modified $PbTiO_3$ ceramics, *Bull. Mater. Sci*. **16**, 679 (1993).
[40]K. Prasad, R. Sati, R. N. Chodhary, and K. L. Yadav, (Pb,Ca) $[(Mn0.05W0.05)Ti0.90]O_3$: X-ray and dielectric studies, *J. Mater. Sci. Lett*. **12**, 758 (1993).
[41]M. Arora *et al.*, Evidence of finite magneto-electric coupling in $SmFeO_3$–$PbTiO_3$ solid solutions, *J. Magn. Magn. Mater*. **547**, 1 (2022).
[42]W. L. Warren, D. Dimos, G. E. Pike, B. A. Tuttle and M. V. Raymond, Voltage shifts and imprint in ferroelectric capacitors, *Appl. Phys. Lett.* **67**, 866 (1995).
[43]A. Morelli, S. Venkatesan and G. Palasantzas, Polarization retention loss in $PbTiO_3$ ferroelectric films due to leakage currents, *J. Appl. Phys.* **102**, 084103 (2007).
[44]J. Mendiola, B. Jimenez, C. Alemany, L. Pardo and L. Del Olmo, Influence of calcium on the ferroelectricity of modified lead titanate ceramics, *Ferroelectrics* **94**, 183 (1989).
[45]L. Yang *et al.*, Perovskite lead-free dielectrics for energy storage applications, *Prog. Mater. Sci.* **102**, 72 (2019).
[46]T. Zhang *et al.*, Enhanced electrocaloric analysis and energy-storage performance of lanthanum modified lead titanate ceramics for potential solid-state refrigeration applications, *Sci. Rep.* **8**, 1 (2018).
[47]Z. Ren *et al.*, Room-temperature ferromagnetism in Fe-doped $PbTiO_3$ nanocrystals, *Appl. Phys. Lett.* **91**, 063106 (2007).
[48]V. R. Palkar, D. C. Kundaliya, S. K. Malik and S. Bhattacharya, Magnetoelectricity at room temperature in the $Bi0.9–xTbxFeO_3$ system, *Phys. Rev. B - Condens. Matter Mater. Phys.* **69**, 9 (2004).
[49]M. Kumar and K. L. Yadav, Study of dielectric, magnetic, ferroelectric and magnetoelectric properties in the $PbMnxTi_1–xO_3$ system at room temperature, *J. Phys. Condens. Matter* **19**, 242202 (2007).
[50]M. Singh, J. Singh, M. Kumar and S. Kumar, Investigations on multiferroic properties of lead free (1–*x*)BCZT-*x*CZFMO based particulate ceramic composites, *Solid State Sci.* **108**, 106380 (2020).